Geophysical Journal International

Geophys. J. Int. (2016) **204,** 1518–1530 doi: 10.1093/gji/ggv526
GJI Geodynamics and tectonics

A free surface capturing discretization for the staggered grid finite difference scheme

T. Duretz,[1] D.A. May[2] and P. Yamato[3]

[1]*Institut des Sciences de la Terre, Bâtiment Géopolis, Lausanne, Switzerland. E-mail: thibault.duretz@unil.ch*
[2]*Institute of Geophysics, ETH Zürich, Zürich, Switzerland*
[3]*Géosciences Rennes, Université de Rennes* 1*, CNRS UMR* 6118*, France*

Accepted 2015 December 7. Received 2015 November 26; in original form 2015 July 12

SUMMARY

The coupling that exists between surface processes and deformation within both the shallow crust and the deeper mantle-lithosphere has stimulated the development of computational geodynamic models that incorporate a free surface boundary condition. We introduce a treatment of this boundary condition that is suitable for staggered grid, finite difference schemes employing a structured Eulerian mesh. Our interface capturing treatment discretizes the free surface boundary condition via an interface that conforms with the edges of control volumes (e.g. a 'staircase' representation) and requires only local stencil modifications to be performed. Comparisons with analytic solutions verify that the method is first-order accurate. Additional intermodel comparisons are performed between known reference models to further validate our free surface approximation. Lastly, we demonstrate the applicability of a multigrid solver to our free surface methodology and demonstrate that the local stencil modifications do not strongly influence the convergence of the iterative solver.

Key words: Numerical solutions; Dynamics of lithosphere and mantle; Mechanics, theory, and modelling.

1 INTRODUCTION

Formally, the surface of the Earth (delimited on top by the atmosphere) corresponds to an interface along which both shear and normal stresses vanish and, hence, deforms freely in response to the motion of the material located below such as, for instance, tectonic processes (Hager *et al.* 1985). Dynamic processes occurring in the crust, lithosphere, and/or deeper in the mantle, have a strong influence on the topographic evolution (e.g. dynamic topography associated with slab detachment, Duretz *et al.* 2011a). Conversely, the development of topography generates buoyancy forces that affect the lithosphere (Willett 1999) and mantle dynamics (Gurnis *et al.* 1996). Furthermore, the presence of such a 'free surface' appears to be a crucial ingredient within the plate tectonics framework by controlling, for instance, the initiation of single-sided subduction zones at convergent plate boundaries (Crameri *et al.* 2012b). This interface also constitutes the place where surface processes (erosion and deposition) occur and can, depending on their nature and efficiency, affect tectonic behaviour (e.g. Willett 1999; Braun & Yamato 2010). Unravelling the interactions between mantle circulation, crustal/lithosphere deformation and the evolution of the Earth's surface thus constitutes a long standing objective in geodynamics. In order to address this issue, the geodynamic community has developed numerical modelling tools specifically designed to study the coupling between tectonic processes and topographic evolution.

In considering grid based geodynamic simulations, the evolution of Earth's surface can be modelled using either conforming, or non-conforming computational meshes. A method employing a mesh which conforms to the topography implies that edges (or faces in 3-D) of the cells within the mesh are aligned with the interface.

Conforming mesh based methods employ either a Lagrangian framework or an Arbitrary Lagrangian–Eulerian (ALE) framework. In the Lagrangian approach, the computational mesh is advected with the fluid velocity (Fig. 1A). An evolving topography is explicitly tracked via the nodes of the mesh, thus the computational grid may require frequent re-meshing procedures in order to maintain solution accuracy (Poliakov & Podladchikov 1992). In the ALE framework, the surface of the mesh advects with the fluid velocity while the coordinates of the interior nodal points are adapted in a manner to preserve mesh quality without consideration of the fluid velocity (Fig. 1B). A re-meshing procedure is required along the explicit surface being tracked and within the interior of the domain. The nature of the ALE formulation allows a structured mesh to be used. While a re-meshing procedure is required, the process is considerably simplified compared to the case of an unstructured mesh. For this reason ALE approaches represent an attractive alternative to model topographic evolution (Fullsack 1995). Both Lagrangian and ALE approaches are standard for finite element and finite volume discretizations. Moreover, these methods offer a natural treatment of the free surface boundary condition.

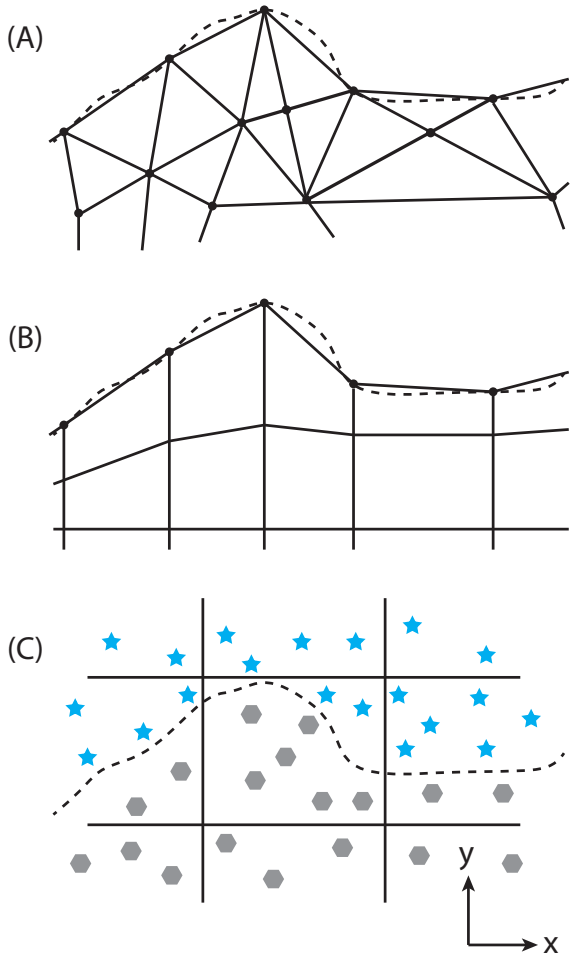

Figure 1. Classification of methods employed to model a free surface (here in dashed line). (A) Lagrangian body fitted mesh, (B) arbitrary Lagrangian–Eulerian (ALE) mesh, (C) marker-in-cell (MIC) method employing a uniformly spaced structured mesh.

In the case of a non-conforming approach, the numerical grid is typically Eulerian and therefore cannot adapt to an evolving topography. A free slip boundary condition can be imposed at the top of the model. In this case, a dynamic topography can be derived from the normal stress resulting from mantle dynamics and acting on the free slip surface assuming instantaneous adjustment of topography (McKenzie 1977). This method however does not take into account the effect of time-dependent redistribution of topographic loads on mantle dynamics. This limitation was circumvented by some authors (e.g. Gurnis *et al.* 1996; Zhong *et al.* 1996) using the computed dynamic topography to define a vertical topographic load (normal stress) distributed along the free surface, thereby allowing a transient influence of dynamic topography on mantle flow. This approach captures vertical topographic displacements but not horizontal components. The latter can be however important in numerous geodynamic contexts (e.g. trench retreat and advances in a subduction zone).

An alternative non-conforming interface method which approximates the free surface boundary condition is the 'sticky air' approach (Schmeling *et al.* 2008; Crameri *et al.* 2012a). The sticky air method is defined by introducing a layer of low viscosity and low density material on top of the model (blue stars in Fig. 1C). The term 'sticky air' comes from the fact that, for practical reasons, the viscosity of this weak layer is usually on the order of 10^{17}–10^{19} Pa s, which is unrealistically large in comparison to true air viscosity. The sticky air method can however reasonably approximate free surface geodynamic flows (e.g. Schmeling *et al.* 2008; Crameri *et al.* 2012a). While it is common to define the sticky air layer on set of Lagrangian markers, it is also possible to track the interface between the sticky air and the lithosphere using a level set representation (e.g. Hillebrand *et al.* 2014).

The sticky air method has several advantages: (i) including a sticky air layer only requires the definition of an additional material phase, its implementation is therefore straightforward; (ii) when the sticky air method is used in combination with Lagrangian markers, the method is naturally sensitive to subgrid topography variations. In other words, topographic variations that are below the numerical mesh resolution can, to some extent, influence the flow below the surface (see case 1 of Crameri *et al.* 2012a). This is an attractive feature for mantle circulation models in which the spatial resolution of the mesh is usually, at most, on the order of 1 km.

Despite the simplicity of the sticky air method, the approach suffers from a number of limitations:

(i) The sticky air layer is represented by a finite volume of material located above the free surface. As such, the sticky air method naturally extends the size of the computational domain and thus introduces additional degrees of freedom which in turn increases the computational cost associated with solving the discrete problem.

(ii) The accuracy of the free surface approximation is highly dependent on the viscosity of the air and the thickness of the air layer (Crameri *et al.* 2012a). *A priori* estimates of the quality of the sticky air approximation can be derived for idealized model configurations (Crameri *et al.* 2012a). However, given an arbitrary initial condition, it is difficult to evaluate the quality of the free surface approximation.

(iii) The sticky air is characterized by a low viscosity material, hence the air/lithosphere interface exhibits a strong viscosity jump. Large and sharp viscosity contrast ($\eta^* \approx 10^2-10^3$) are known to deteriorate the convergence of iterative methods used to solve the discrete flow problem (May & Moresi 2008; Tackley 2008). It is thus preferable to avoid the use of sticky air when using iterative schemes (i.e. geometric multigrid). Nonetheless iterative solvers are preferable over direct solver when modelling mantle convection, or lithospheric deformation in 3-D.

(iv) The treatment of surface processes with the sticky air method can be cumbersome since the method does not explicitly define the location of the free surface. Instead, the topographic profile must be inferred by region of space defined between the material points defining the crust and the material points defining the sticky air. Within the geodynamic community, there is no agreement on the manner to extract the coordinates of the free surface from a sticky air implementation. Moreover, when markers are used to represent the sticky air, the position of the markers located in the vicinity of the sticky air/crust implicit interface fluctuates. This issue known as the 'marker fluctuation' problem (Crameri *et al.* 2012a) necessitates additional treatments.

(v) Under certain conditions, fluid motion within the sticky air layer can be much faster than that within the lithosphere. This can therefore lead to drastic time-step restrictions, and in the worse case lead to unphysical dynamics near the surface.

(vi) If Lagrangian markers are employed to track the sticky air layer, it is common that the air markers will be entrained within the lithosphere (e.g. along a subduction interface; Schmeling *et al.* 2008). While air entrainment is fluid-dynamically consistent with

the mathematical model, it is however geomechanically inconsistent. Hence, in the event of air entrainment, ad-hoc treatments must be adopted to remove the entrained air markers.

(vii) In thermomechanical simulations, the treatment of the boundary conditions for the conservation of energy at the free surface is not straightforward. Thermal parameters of the sticky air (i.e. conductivity, specific heat) need careful investigation in order impose the desired boundary condition (i.e. constant temperature or heat flux).

To address the short-comings of the sticky air method, we propose a new interface capturing technique specifically designed for the staggered grid finite difference scheme. The key idea of the interface capturing scheme is to (i) approximate the free surface interface via a staircase-like interface which conforms with the edges of the control volumes, and then (ii) locally modify the finite difference stencil along the staircase boundary to enforce the required free surface boundary condition. The structure of the paper is as follows. First, we describe the governing equations and the discretization of the free surface boundary condition. We then demonstrate the validity of the method by (i) showing that the free surface boundary condition is grid-convergent and (ii) reproducing results from free surface benchmarks used by the geodynamic community. Lastly, we discuss the technical and practical implications of the free surface discretization, as well as its limitations.

2 MATHEMATICAL MODEL

For the purpose of modelling mantle and lithosphere dynamics, we consider that material deformation is governed by the Stokes equations

$$\frac{\partial \tau_{ij}}{\partial x_j} - \frac{\partial p}{\partial x_i} = \rho(\boldsymbol{x}) g_i, \tag{1}$$

where τ_{ij} represents the deviatoric stress tensor, p is the total pressure, g_i is the gravity vector and ρ is the material density. In this work, we employ a linear viscous rheology, thus the deviatoric stress tensor is related to the deviatoric strain rate tensor $\dot{\epsilon}'_{ij}$ via:

$$\tau_{ij} = 2\eta(\boldsymbol{x})\dot{\epsilon}'_{ij}, \tag{2}$$

where η is the dynamic viscosity. In the following applications, the viscosity and density vary in space, however the value at material points is constant throughout time, for example,

$$\frac{D\eta}{Dt} = 0, \quad \frac{D\rho}{Dt} = 0. \tag{3}$$

The following formulation of the free surface boundary condition is also valid for fluids with time-dependent density and viscosity (e.g. temperature and pressure-dependent). For the geodynamic applications under consideration, we assume that the fluid is incompressible and thus we employ the following statement for the conservation of mass:

$$\frac{\partial v_i}{\partial x_i} = 0, \tag{4}$$

in which v_i represents the velocity vector. We note that under the assumption of incompressibility, the total strain rate tensor $\dot{\epsilon}_{ij}$ is equal to the deviatoric strain rate tensor. Eq. (2) hence reduces to $\tau_{ij} = 2\eta(\boldsymbol{x})\dot{\epsilon}_{ij}$.

The conservation of momentum (eq. 1) and mass (eq. 4) define the evolution of velocity and pressure within a time-dependent domain Ω. Considering velocity and pressure as primitive variable, uniqueness of the solutions are obtained through supplementing the conservation equations with one of the following boundary conditions at every point $\boldsymbol{x}$ contained on the boundary $\partial\Omega$;

(1) Dirichlet (prescribed normal and tangential velocity components):

$$v_i = \bar{v}_i \quad \text{on } \partial\Omega_{\mathrm{D}}. \tag{5}$$

(2) Neumann for prescribed normal stress components:

$$n_i(\tau_{ij} - p\delta_{ij})n_j = \bar{\sigma} \quad \text{on } \partial\Omega_{\mathrm{N}}, \tag{6}$$

where n_j is the outward pointing unit normal vector from the boundary $\partial\Omega$.

(3) Neumann for prescribed shear stress component:

$$t_i \tau_{ij} n_j = \bar{\tau} \quad \text{on } \partial\Omega_{\mathrm{N}}, \tag{7}$$

where t_i is the unit tangent vector to the boundary $\partial\Omega$.

(4) Dirichlet-Neumann (prescribed normal velocity and tangential stresses):

$$v_i n_i = \bar{v}_n, \quad t_i \tau_{ij} n_j = \bar{\tau} \quad \text{on } \partial\Omega_{\mathrm{DN}}, \tag{8}$$

where t_j is the unit vector tangential to the boundary $\partial\Omega$.

From these general boundary condition definitions, the following choices lead to the following boundary conditions used in geodynamic simulations: (i) choosing $\bar{v}_i = 0$ results in a 'no-slip' boundary condition; (ii) a 'free surface' boundary condition is obtained by choosing $\bar{\sigma}_i = 0$ and $\bar{\tau}_i = 0$; (iii) setting $\bar{v}_n = 0$, $\bar{\tau}_i = 0$ yields a 'free-slip' boundary condition.

3 NUMERICAL METHOD

The Stokes (eq. 1) and continuity equations (eq. 4) are discretized using the finite difference method on a staggered grid in 2-D (Harlow & Welch 1965). This type of discretization is commonly used in the geodynamic community (e.g. Tackley 2008; Gerya 2010; Furuichi *et al.* 2011) as (i) the staggered arrangement of the primitive variables (v_i, p) satisfies the inf-sup stability criterion (i.e. no spurious pressure modes) (Shin & Strikwerda 1997) and (ii) the stencil associated with the discrete operators contains few entries (11 in 2-D, 17 in 3-D), thereby reducing memory requirements and floating point operations. In case of smooth spatial variations of material properties (i.e. viscosity and density), the staggered grid offers second order spatial accuracy. In the presence of material discontinuities across the control volumes, the accuracy of the staggered grid is first order accurate (Deubelbeiss & Kaus 2008; Duretz *et al.* 2011b). The standard staggered grid discretization is however restricted to using grids which are orthogonal to the coordinate system (e.g. Cartesian, cylindrical, spherical). Such a restriction imposes strong limitations on its geometric flexibility and, subsequently, on the ability to represent time-dependent free surface geometries.

4 FREE SURFACE DISCRETIZATION

In this section, we describe an implementation of the free surface boundary condition which can resolve topographic profiles that are not aligned with our finite difference (FD) grid. Given previous work examining the order of accuracy of the staggered grid FD discretization in the presence of discontinuous viscosity structures, our main goal is to design a free surface boundary condition which is at least first order accurate. A secondary objective of our implementation is that it can be readily implemented into existing FD geodynamic numerical codes.

To that end, we propose to represent the free surface boundary condition on a structured Eulerian grid, with the topography discretized in a staircase manner. In practice the procedure can be divided into two steps: (i) the identification of the cells ('cell flagging') that are below the free surface and, (ii) the introduction of local stencil modifications which need to be applied at the surface cells to enforce the vanishing stress boundary condition. One should note that the overall approach shares a number of similarities with the original work of Harlow & Welch (1965).

4.1 Cell flagging

We assume that the free surface is defined by a contour $\phi(\boldsymbol{x})$ and that there exists a mean to query whether a point $\boldsymbol{x}_i$ is 'inside' the contour ϕ (fluid domain) or 'outside' the contour. In other words, $\phi(\boldsymbol{x})$ corresponds to the y coordinate of the free surface for any given x coordinate. We identify as active cells ('A-cells') the fluid-filled cells which have a centroid $\boldsymbol{x}_c$ inside the contour ϕ (Fig. 2A). The velocity and pressure degrees of freedom of the active cells will be included in the discrete solution. Cells not identified as A-cells are flagged as void cells ('V-cells'). The degrees of freedom associated with cells which are not identified as active are not part of the discrete solution. Any neighbour cell n of an A-cell which is not an A-cell is labelled as an interface cell (I-cell) (open circles in Fig. 2A). The pressure degree of freedom associated with I-cells are used to enforce a zero pressure Dirichlet boundary condition.

4.2 Stokes stencil modification

Once both the active and interface cells have been identified, the Stokes and continuity equations can be discretized while taking into account a free surface boundary condition. Whereas the discretization of the continuity equation remains unchanged, the stencils corresponding to the momentum equations require some modifications. In the cells that are located along the free surface (I-cells), a typical 11 nodes stencil cannot be assembled in 2-D as all the velocity nodes located above the surface are deactivated (Figs 2B and C). Instead we use the free surface constraints to discretize the momentum equations which imply that both the normal stresses (σ_{xx}, σ_{yy}) and the shear stress (τ_{xy}) should vanish at the free surface. The pressure gradient across the free surface can be evaluated in the usual manner as the pressure node in any adjacent I-cell is defined as a Dirichlet boundary condition. The general stencil for the x-momentum equation can be spelled as:

$$F_u = \frac{1}{h_x}\left(\tau_{xx}^{\mathrm{E}} - \tau_{xx}^{\mathrm{W}}\right) + \frac{1}{h_y}\left(\tau_{xy}^{\mathrm{N}} - \tau_{xy}^{\mathrm{S}}\right) - \frac{1}{h_x}\left(p^{\mathrm{E}} - p^{\mathrm{W}}\right) - F^x_{\mathrm{Dirichlet}} - F^x_{\mathrm{Neumann}}, \quad (9)$$

where F_u represents the residual of the x-momentum equation, h_i stands for the grid spacing and the superscripts E, W, N, S corresponds to the cardinal directions. The terms $F^x_{\mathrm{Dirichlet}}$ and F^x_{Neumann} correspond to contributions from the Dirichlet and Neumann boundary conditions respectively. For the interface geometry depicted in Fig. 2(B), the modified stencil can written as:

$$F_u = \frac{1}{h_x}\left(-\tau_{xx}^{\mathrm{W}}\right) + \frac{1}{h_y}\left(-\tau_{xy}^{\mathrm{S}}\right) - \frac{1}{h_x}\left(p^{\mathrm{E}} - p^{\mathrm{W}}\right) - F^x_{\mathrm{Dirichlet}} - F^x_{\mathrm{Neumann}}, \quad (10)$$

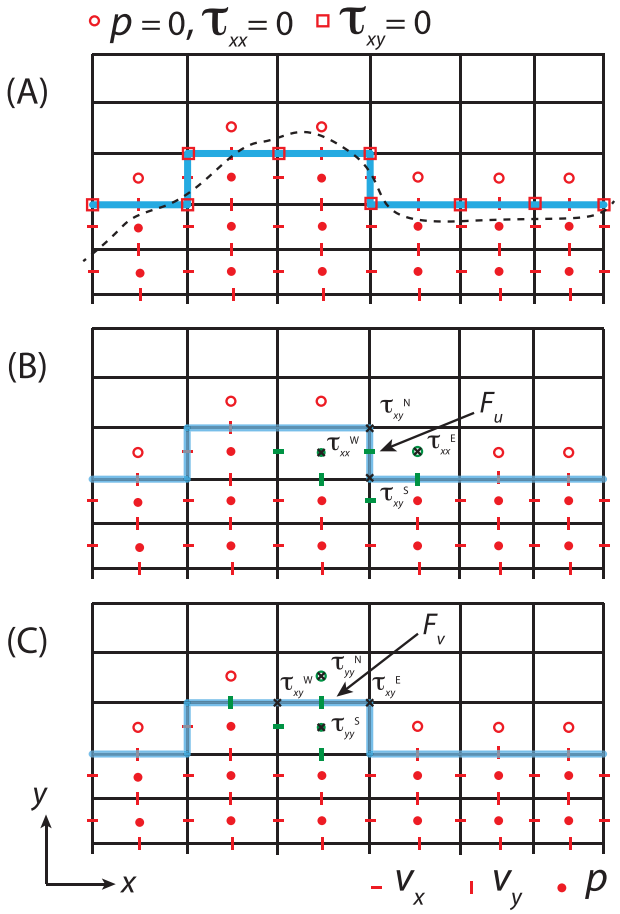

Figure 2. (A) Cell flagging scheme for the free surface boundary conditions. The black dashed line represents the topographic function $\phi(x)$, the blue line represents the corresponding staircase topography. Above the blue line, degrees of freedoms are not activated, except for the first row of pressure nodes (open red circles), which correspond to zero pressure Dirichlet boundary conditions. Below the blue line, filled circles and bars represent activated pressure and velocity degrees of freedom. Open red squares and stars indicate the location of the surface stress tensor components. These nodes are not explicitly included in the system of equations (i.e. they are not additional degrees of freedoms) but are used to enforce the free surface stencil. (B) Stencil corresponding to the x component of the momentum balance equation (eq. 1). The green symbols correspond to nodes required to evaluate the equation at the given location (F_u). The black crosses indicate the deviatoric stress tensor components involved in the calculation of F_u. (C) Same as (B) but for the y-momentum balance equation (F_v).

assuming that $\tau_{xx}^{\mathrm{E}} = 0$ and that $\tau_{xy}^{\mathrm{N}} = 0$ since both velocity gradients across the free surface which contribute to the shear stress $\tau_{xy}^{\mathrm{N}} = \eta^{\mathrm{N}}(\frac{\partial v_x}{\partial y} + \frac{\partial v_y}{\partial x})^{\mathrm{N}}$ vanish. In the case the surface would be horizontal the expression of τ_{xy}^{N} would be $\tau_{xy}^{\mathrm{N}} = \eta^{\mathrm{N}}(\frac{\partial v_y}{\partial x})^{\mathrm{N}}$, as only the vertical velocity gradient would vanish. Respectively, in the case of a vertical surface, the shear stress would take the form of $\tau_{xy}^{\mathrm{N}} = \eta^{\mathrm{N}}(\frac{\partial v_x}{\partial y})^{\mathrm{N}}$. For τ_{xy}^{S}, the four velocity nodes involved in the evaluation of the two velocity gradients are contained within the computational domain, its calculation remains unchanged. Similar stencil modifications can further be applied to the y component (Fig. 2C). The unmodified stencil corresponding to the y-momentum equation is spelled

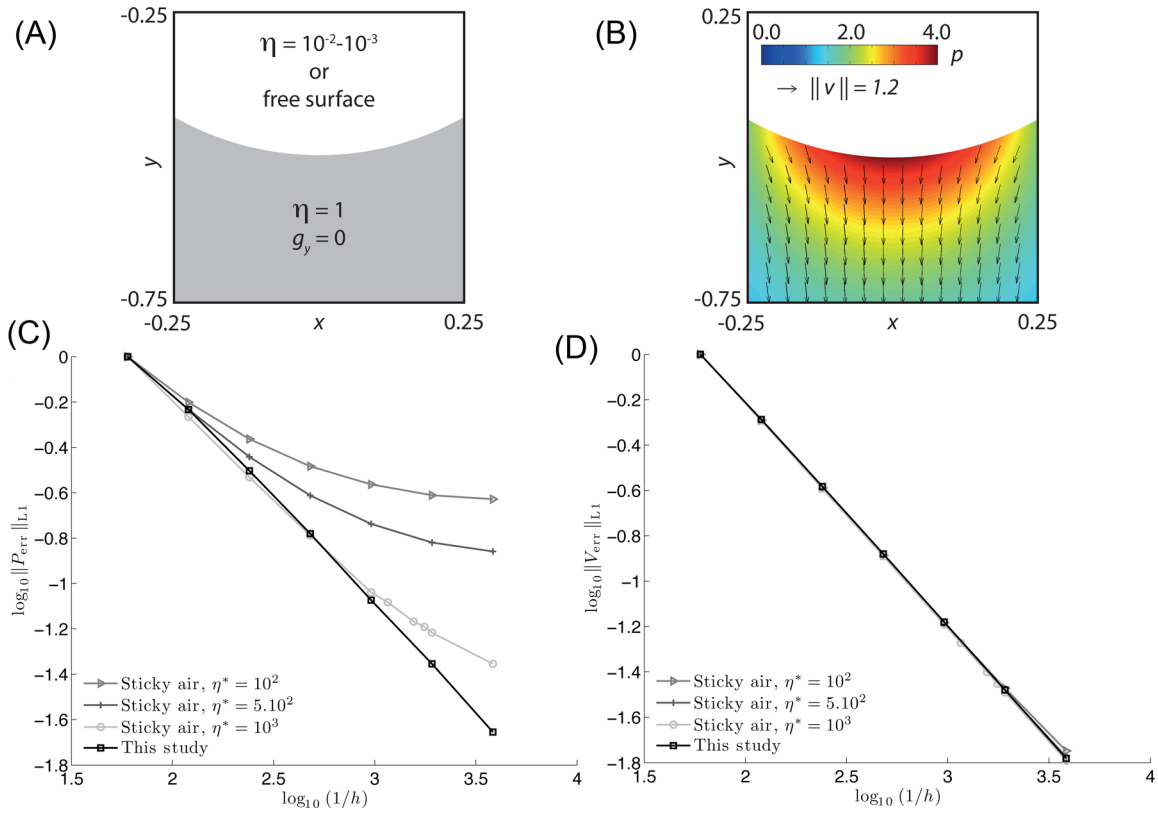

Figure 3. Convergence of the free surface boundary condition and sticky air method with decreasing grid size h. (A) Model configuration used for the convergence test. (B) Pressure and velocity fields from the analytic solution. (C,D) Pressure and velocity errors (L_1 norm) for both the free surface boundary condition and the sticky air approach. For the sticky air models, the viscosity contrast is denoted via η^*. The results were computed using 6×6 markers per cell.

as:

$$F_v = \frac{1}{h_y}\left(\tau_{yy}^{\mathrm{N}} - \tau_{yy}^{\mathrm{S}}\right) + \frac{1}{h_x}\left(\tau_{yx}^{\mathrm{E}} - \tau_{yx}^{\mathrm{W}}\right) - \frac{1}{h_y}\left(p^{\mathrm{N}} - p^{\mathrm{S}}\right) - \rho g_y - F^y_{\mathrm{Dirichlet}} - F^y_{\mathrm{Neumann}}, \quad (11)$$

where g_y corresponds to the vertical component of the gravitational acceleration vector. The modified stencil is given by:

$$F_v = \frac{1}{h_y}\left(-\tau_{yy}^{\mathrm{S}}\right) + \frac{1}{h_x}\left(\tau_{yx}^{\mathrm{E}}\right) - \frac{1}{h_y}\left(p^{\mathrm{N}} - p^{\mathrm{S}}\right) - \rho g_y - F^y_{\mathrm{Dirichlet}} - F^y_{\mathrm{Neumann}}, \quad (12)$$

assuming that both τ_{yy}^{N} and τ_{yx}^{E} vanish. We note that these stencil modifications do not alter the symmetry of the resulting discrete Stokes operator.

In this work, the discrete velocity and pressure solutions are obtained by sparse direct factorization of the discrete Stokes operator. The benefits of the free surface boundary condition in the context of iterative solvers are discussed and exemplified in Section 8.1.2.

5 ACCURACY OF THE SCHEME

The accuracy of the proposed free surface discretization is evaluated by comparing with the analytic solution of Schmid & Podladchikov (2003). This analytic solution is used as it is valid in the limit when the inclusion viscosity vanishes (i.e. it is inviscid). Under this condition, normal and shear stresses vanish at the matrix/inclusion interface and the pressure in the inclusion vanishes. This configuration provides equivalent boundary condition as that used to describe a free surface. Moreover, the interface in this analytic solution is curved, and therefore it is non-trivial to resolve using an orthogonal mesh—a scenario which reflects the general case of interest involving non-flat topography.

Here we use the same approach as in Duretz *et al.* (2011b) where we determine the order of accuracy of the discretization by computing velocity and pressure errors for different grid resolutions. The pressure discretization error (evaluated in the L_1 norm) we use is given by:

$$\|p_{\mathrm{err}}\|_{L_1(\Omega)} = \frac{1}{V}\int_\Omega |p - p^h|\, dV, \quad (13)$$

where p^h is the numerical solution, p is the analytic pressure field, and V corresponds to the volume of the computational domain Ω.

We define an inviscid inclusion centred at (0, 0) with radius $r = 0.5$ and employ a model domain defined by $\Omega = [-0.25, 0.25] \times [-0.75, -0.25]$. The chosen model domain thus contains a curved segment of the inclusion, thereby mimicking a free surface (see Fig. 3A). The viscosity of the matrix (below the surface) is set to 1. In the numerical simulation, the coordinates of the material interface are used to initialize the topographic function on which the free surface boundary condition is enforced. We use Dirichlet boundary conditions for the lateral and bottom boundaries, which receive normal and tangential velocity values evaluated with the analytic solution. The grid convergence test is carried out on a sequence of seven grids using $N \times N$ control volumes, where $N = \{30, 60, 120, 240, 480, 960, 1920\}$. The side lengths of each control volume (h_x, h_y) are equal and will simply be denoted via h.

In Fig. 3(C) we report how the pressure discretization error varies with decreasing grid spacing. The pressure error is observed to decrease linearly with decreasing grid spacing h. The slope of this line is -1.001, which indicates that the pressure approximation is first order accurate in L_1. We also report first order accuracy for the velocity discretization error (Fig. 3D). Additionally, we carried out a similar test using the sticky air approach. In these tests, the material above the curved interface was considered as a less viscous sticky air and along the top of the model domain we prescribed a velocity Dirichlet boundary condition given by the analytic solution. In Fig. 3(C) we also report the measured L_1 pressure error obtained using viscosity contrasts η^* which reflect those commonly by the community when adopting the sticky air approximation. Whereas first order accuracy was obtained for velocity errors (Fig. 3D, pressure errors are observed to stagnate with decreasing grid spacing. The supplied script (FreeSurfaceAccuracyTest.m) can be used to reproduce the grid convergence using the free surface boundary condition.

6 TIME-DEPENDENT FREE SURFACE EVOLUTION

One of the main interests of direct numerical models is to track deformation with time. This is particularly important concerning the free surface because topography constitutes one of the first order feature of the models that can be compared with natural observations. Since different methods can be used (e.g. level set functions), we briefly describe our tracking method here. Further details can be found in Appendix A.

The free surface $\phi(\boldsymbol{x}, t)$ evolves temporally according to

$$\frac{\partial \phi}{\partial t} + \boldsymbol{v} \cdot \nabla \phi = 0 \quad \rightarrow \quad \frac{D\phi}{Dt} = 0, \tag{14}$$

subject to the initial condition $\phi(\boldsymbol{x}, 0) = \phi^*(\boldsymbol{x})$.

We will classify methods to represent the free surface as either 'explicit' or 'implicit'. Explicit methods track the coordinates of ϕ, while implicit methods indirectly define the location of the interface. With an implicit interface representation, a reconstruction is required if the coordinates of the interface are needed. The following techniques are all of the implicit variety: level sets (Suckale *et al.* 2010), volume of fluid, particles level set method (Samuel & Evonuk 2010), phase field methods, or marker-in-cell (MIC) as long as the markers are used for tracking volumes (Weinberg & Schmeling 1992). Explicit methods are by definition generally Lagrangian schemes, with notable examples being: the marker-chain approach of van Keken *et al.* (1997), contour tracking, front-tracking using meshes fitted to the interface.

Here we have used a combination of the different techniques listed above. We have chosen to (i) discretize ϕ using the marker chain approach (van Keken *et al.* 1997) and to (ii) discretize material below the free surface using a MIC approach. The markers used to discretize the free surface and the volume domain are advected using fourth order accurate in space first order in time Runge–Kutta (RK4) method. A standard bilinear node to marker interpolation (Gerya 2010) is used to define the velocity at each marker coordinate. Following the advection of all markers, we use the surface markers to reconstruct a continuous function (C_0 continuity) corresponding to a piecewise linear representation of ϕ within each control volume (see Appendix A). The reconstruction uses standard distance-weighted linear interpolation (Gerya 2010). The reconstructed surface $\hat{\phi}$ is used to 'remesh' the surface markers through uniform re-sampling within each control volume. Furthermore, $\hat{\phi}$ is used to define subgrid variations in topography through a fluid volume weighted correction which we describe in Section 6.1.

As is common in geodynamic modelling, we assume the coupling between the surface evolution (eq. 14) and the conservation of momentum and mass for the fluid (eqs 1 and 4) is weak and thus we solve these two systems in de-coupled (explicit) fashion. Specifically, at each time step, we solve the conservation of momentum and mass for the fluid velocity ($\boldsymbol{v}^h$) and pressure (p^h). The resulting velocity is then used to update the discrete form of eq. (14), which requires performing an RK4 step to update the surface markers coordinates (see Appendix A for further details).

6.1 Subgrid topographic sensitivity

The staircase free surface representation described in Section 4 is inherently dependent on the vertical and horizontal spacing. In cases where the amplitude of topographic variations is below the grid resolution, the latter would not be captured by the discretization and could not possibly influence the flow field. In order to circumvent this aspect, we introduce a surface density correction. The density in the surface cells is thus modified by the relative volume of fluid present in the current cell:

$$\rho_i^{\text{eff}} = \rho_i \frac{V_f}{h_x h_y}, \tag{15}$$

where ρ_i^{eff} correspond to the corrected density evaluated at the cell centre, ρ_i is the real material density, and V_f corresponds to the volume of fluid in the current cell. This quantity is evaluated by integrating the topography function $\hat{\phi}$ using a one point quadrature rule. The influence of this surface density correction is emphasized in Section 7.1.

7 COMPARISON WITH COMMUNITY BENCHMARKS

7.1 Topography benchmark

We first consider the two test cases presented in Crameri *et al.* (2012a). Both cases were designed to study the evolution of topography above a two-layer system (lid, mantle) in the presence of gravity (see fig. 1 of Crameri *et al.* 2012a, for the initial model configuration).

7.1.1 Case 1

In the first case, the initial topography is characterized by a cosinusoidal perturbation. This perturbation provides the driving force for viscous relaxation and the topography tends to flatten out with time. We ran models using a grid resolution of 100×100 cells, six surface markers per cell column and a constant time step (CTS, $\Delta t = 5 \times 10^9$ s) and tested the influence of the surface density correction. The time-step value is chosen such that it is smaller than the viscous relaxation time corresponding to this test (14.85 kyr or 4.74×10^{11} s, *cf.* Crameri *et al.* 2012a). The maximum topography is recorded every five time steps and is compared against results previously obtained with the codes MILAMIN_VEP (Kaus 2010) (which uses a free surface) and STAGYY (Tackley 2008) (which uses the sticky air approximation). The comparison between the different models is depicted in Fig. 4 (*cf.* fig. 2 of Crameri *et al.* 2012a). The model that was run with the surface density correction (see Section 6.1) shows good agreement with MILAMIN_VEP (Kaus 2010) and

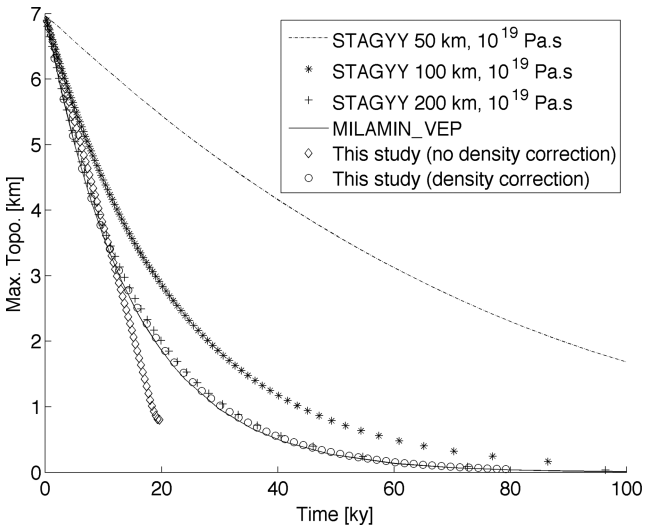

Figure 4. Case 1 topography benchmark of Crameri *et al.* (2012a). Models were computed with and without subgrid density correction. Reference results of STAGYY (using three different sticky air layer thickness) and MILAMIN_VEP (free surface) are shown for comparison.

the STAGYY (Tackley 2008) simulation which used a sticky air layer thickness and viscosity of 200 km and 10^{19} Pa s respectively. We observed that neglecting the surface density correction does not provide an accurate evolution of topography. In this case, the maximum topography clearly deviates from the benchmark results as the amplitude of topographic variations is lower than the vertical grid spacing ($h_y = 7$ km).

7.1.2 Case 2

In the second case, the topography is initially flat and a buoyant inclusion is located within the mantle. The flow induced by the rise of the buoyant inclusion causes the development of topography. In this test, we monitor the evolution of the maximum topography over a 20 kyr time period and compare it to the solution obtained with the code MILAMIN_VEP which we consider as a reference model (Fig. 5; *cf.* fig. 6 of Crameri *et al.* 2012a). We carried out six numerical models in total, in the first series of three simulations we used two different spatial resolutions (300 × 200 cells and 400 × 300 cells). The simulations were run with adaptive time stepping (ATS) and using a Courant number (C) given by

$$C = \Delta t \left(\frac{\max(v_x, v_y)}{\min(h_x, h_y)} \right) = \frac{1}{2}.$$

Models which were run with surface density correction compare well with the reference model (Fig. 5A). The model computed with the highest resolution shows the best agreement with the reference solution. On the other hand, the simulation performed without surface density correction fail to reproduce the results of the reference model. This further emphasizes the importance of considering subgrid topographic variations. The second series of three simulations were conducted using a mesh resolution of 300 × 200 cells, 6 surface markers per cell column, and three different CTS value. The three models take into account the surface density correction. The evolution of the maximum topography is depicted in Fig. 5(B), in which the focus is set on the initial stages of topographic build up (<1 Myr). Whereas the models computed with the largest time step tend to initially undershoot the reference topography, we observe that decreasing the size of the time step leads to a closer agreement with the reference solution.

7.2 Free surface Rayleigh–Taylor instability

Here we consider the topographic evolution generated by a convecting two fluid system driven by buoyancy variations. The free surface Rayleigh–Taylor instability is initiated by prescribing an

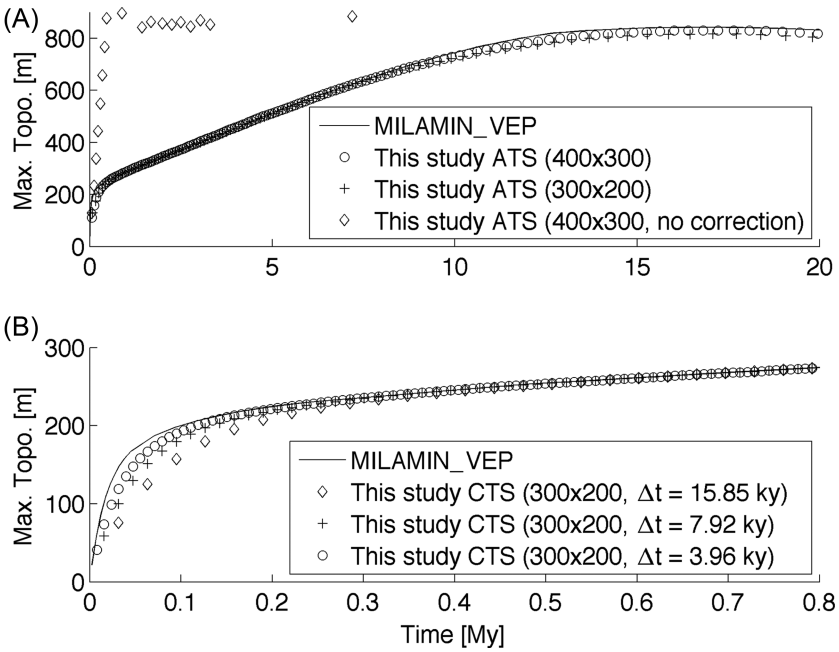

Figure 5. Case 2 topography benchmark of Crameri *et al.* (2012a). (A) Long-term evolution of the maximum topography over 20 kyr. Models were calculated with and without subgrid density correction. An adaptive time stepping (ATS, $C = 0.5$) strategy was employed. (B) Topographic evolution in the early stages of the simulation (isostatic timescale). Models were computed using constant time step (CTS). The reference results of MILAMIN_VEP are plotted in each panel.

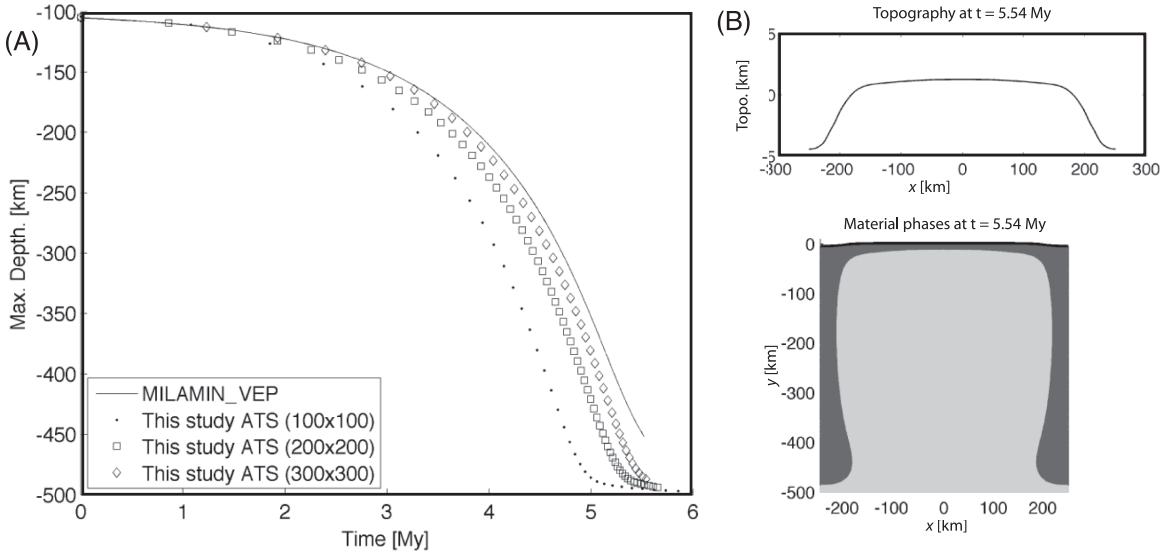

Figure 6. (A) Rayleigh–Taylor instability test. Simulations were run using three different grid resolutions and adaptive time stepping (ATS). The results of Kaus *et al.* (2010) (solid line) were computed using a body-fitted finite element method (MILAMIN_VEP) that serves as an accurate reference model. (B) Topography and material phases after 5.54 Myr of simulation time for model ATS with resolution 300 × 300 cells. Dark grey corresponds to the dense lid whereas light grey depicts the buoyant diapir. The black line indicates the topography (coordinates of the surface markers).

initial condition of the fluid–fluid interface which is gravitationally unstable. The complete definition of this model is described in Kaus *et al.* (2010). We ran models on three different grid resolutions (100 × 100 cells, 200 × 200 cells, and 300 × 300 cells) using ATS with a Courant number equal to 0.5. The models employed 6 surface markers per cell column and utilized the surface density correction. This model configuration may lead to spurious instability when evolving material fields with an explicit advection scheme (Kaus *et al.* 2010). Implementing a free surface stabilization algorithm was found necessary in order to perform this simulation. Using the free surface stabilization algorithm described in Duretz *et al.* (2011b) together with the free surface boundary condition implies two modifications. Establishing density gradients across the free surface require knowledge of the density above and below the free surface. The density above the free surface can be set to a pre-defined value (air or water density). The density below the surface uses the effective values obtained via the surface density correction (see Section 6.1). Models were run with the stabilization parameter, θ, set to 1.0.The model results are compared against a reference model computed with MILAMIN_VEP (Fig. 6, *cf.* fig. 5 of Kaus *et al.* 2010). We obtain reasonable agreement with the reference model. Our results tend towards the reference model with increasing mesh resolution.

7.3 Subduction benchmark

This case 1 subduction benchmark simulates the initiation of buoyancy-driven subduction, in the absence of upper plate. The topography is initially flat and develops with ongoing subduction and the trench migrates laterally due to the effect of slab rollback. The initial model configuration is depicted in fig. 1 of Schmeling *et al.* (2008). We ran two different simulations using grid resolution of 200 × 150 cells and 400 × 300 cells, 6 surface markers per cell column and ATS ($C = 0.5$). We track the maximum depth of the slab (i.e. slab tip depth) with time. Our results are compared against those computed with codes employing a free surface, namely LAMEM and FEMS-2D (Schmalholz 2006). Reasonable agreement is achieved between our models and those of LAMEM but strongly differ with those of FEMS-2D (Fig. 7A, *cf.* fig. 10 of Schmeling *et al.* 2008). This discrepancy is explained by the fact that we used arithmetic viscosity averaging (as in LAMEM), whereas no viscosity averaging is used in the FEMS-2D calculation which employs a Lagrangian framework (see discussion in Schmeling *et al.* 2008). Nevertheless, with increased mesh resolution, the results obtained with our method tend towards those of FEMS-2D. The free surface approach well captures the dynamics of topography development associated with the motion of large scale tectonic motions. This behaviour is illustrated in Fig. 7(B), which depicts the location of both trench and forebulge associated with the sinking of the slab into the mantle.

8 DISCUSSION

8.1 Benefits over the sticky air method

The free surface boundary condition described in this work overcomes a number of drawbacks of the sticky air approximation (see Section 1). Our free surface implementation reduces the total number of the degrees of freedom since the velocity and pressure fluid associated with stick air layer do not need to be included in the computational model domain. Subsequently it also reduces the number of Lagrangian markers required (if an MIC approach is adopted) as we do not need to track deformation within the sticky air layer. The free surface discretization does not require calibration nor tuning of parameters unrelated to the physical problem of interest (i.e. thickness of the air layer, material and thermal properties of the air, choice of boundary condition above the sticky air). With a suitable discretization of the interface defining the free surface, our free surface boundary condition implementation will resolve subgrid topographic variations. Moreover, our approach naturally prevents from any entrainment of sticky air markers below the surface of the model, and additionally our approach avoid potential time-step restrictions which might occur due to fast dynamics present within a sticky air layer.

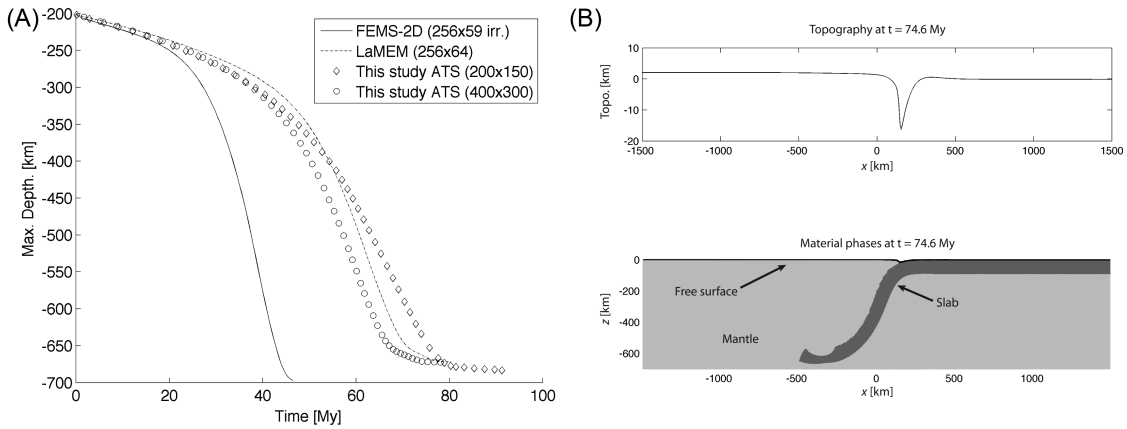

Figure 7. Subduction benchmark of Schmeling *et al.* (2008), Case 1. (A) Simulations of spontaneously retreating subduction were run using two different grid resolutions (see caption). Results computed with FEMS-2D and LAMEM, which also employed a true free surface, are plotted for comparison. (B) Topography (upper panel) and material phases configuration (lower panel) after 74.6 Myr of simulation time (model ATS, 400 × 300 cells). The grey materials represent the lithosphere (dark) and the asthenosphere (light), the black line corresponds to the surface markers depicting the position of the free surface.

8.1.1 Convergence

Our results indicate that the sticky air approximation adopted in many geodynamic simulations is not convergent as the spatial discretization parameter h (size of the control volume) is continually reduced (Fig. 3C). The accuracy of the sticky air approximation depends on both the grid spacing and the viscosity ratio, hence convergence can be recovered by increasing the viscosity contrast together with decreasing the grid spacing. The observed lack of convergence under mesh refinement (at fixed viscosity ratio) can be understood in the following way. Considering a stationary problem with a linear, iso-viscous rheology, then the total error for the numerical simulation can be expressed as:

$$E(\Omega)_{L_1} = \|\boldsymbol{v} - \boldsymbol{v}^h\|_1 + \|p - p^h\|_1 + E_{\mathrm{BC}}^{\mathrm{Dirichlet}} + E_{\mathrm{BC}}^{\mathrm{Neumann}} + E_{\mathrm{solve}}. \quad (16)$$

The first two terms are the usual velocity and pressure errors associated with the discrete solution $(\boldsymbol{v}^h, p^h)$. E_{solve} is the error associated with solving the discrete equations $Ax = b$. $E_{\mathrm{BC}}^{\mathrm{Dirichlet}}$, $E_{\mathrm{BC}}^{\mathrm{Neumann}}$ are the errors associated with the Dirichlet and Neumann type boundary conditions.

Assuming that each term can be expressed as $e_i = C_i h^{n_i}$, where C_i is an unknown constant independent of h, then in the limit of $h \to 0$, $E(\Omega)_{L_1}$ will have an order of accuracy (bounded from above) given by $\mathcal{O}(h^m)$, where $m = \min(n_i)$. That is, the order of accuracy of the method is dominated by the term in eq. (16) which converges the slowest, e.g. the term with the smallest exponent n_i. For example, for $E(\Omega)_{L_1}$ to be first order accurate, we require that all terms in eq. (16) converge at a rate of $\mathcal{O}(h)$ or higher in L_1. From previous work, we know that the velocity and pressure errors converge as $\mathcal{O}(h^2)$ and $\mathcal{O}(h)$. Our implementation of Dirichlet boundary conditions is also known to be $\mathcal{O}(h^2)$ accurate. We have also used an exact sparse direct solver, thus E_{solve} can be taken to be of machine precision (negligible error).

In the context of a sticky air calculation, $E_{\mathrm{BC}}^{\mathrm{Neumann}}$ is connected with the approximation of $\sigma_{ij} n_j = 0$ along the free surface. The quality of the approximation is a function of the values chosen for η_{air} and L_{air} (thickness of the sticky air layer) and is not a function of the mesh resolution h. Thus, in the limit $h \to 0$, $E_{\mathrm{BC}}^{\mathrm{Neumann}} \to Ch^0 =$ constant, thus $E(\Omega)_{L_1}$ has an order of accuracy of $\mathcal{O}(1)$. For the numerical experiments we considered in Section 5, the $\mathcal{O}(1)$ pressure error in the free surface approximation was observed to dominate $E(\Omega)_{L_1}$ when $h \approx 2 \times 10^{-3}$ for the model with $\eta^* = 10^2$.

From numerical experiments, the method proposed in this paper to approximate the free surface is observed to be first order accurate (in L_1). The error in our free surface approximation is purely geometric and stems from our staircase representation of the free surface interface. This geometric error has an order of accuracy of $\mathcal{O}(h)$. The slowest converging terms in eq. (16) are thus associated with the pressure approximation and the Neumann boundary condition approximation, both of which have an $\mathcal{O}(h)$ error. Thus, in the limit of $h \to 0$, $E(\Omega)_{L_1}$ will have an order of accuracy of $\mathcal{O}(h)$.

In addition to the stationary calculations performed in Section 5, the comparisons performed in Sections 7.1–7.3 with time-dependent free surface reference models employed in geodynamics confirm that our free surface treatment possesses both spatial and temporal discretization errors that converge with increasing spatial and temporal resolution.

8.1.2 Applicability of multigrid solvers

Robust convergence of iterative solvers is difficult to obtain when solving Stokes problems with a highly variable viscosity structure (e.g. May & Moresi 2008). Iterative methods are however necessary to solve the discrete Stokes problem associated with high resolution 2-D and 3-D simulations. The inclusion of sticky air layer naturally implies that a large viscosity contrast should be used in a simulation and will thus adversely affect the convergence of iterative solvers. With the free surface boundary condition proposed here, the free surface is imposed as a boundary condition, therefore no viscosity contrast is needed to simulate free surface dynamics.

In order to illustrate this aspect, we have tested the proposed free surface treatment together with an iterative Stokes solver employing the geometric multigrid method described in chap. 14 of Gerya (2010). This method employs V-cycles and relies on a Gauss–Seidel smoother. At each smoothing step, we sweep through grid (horizontal direction first, followed by the vertical direction) and subsequently update velocity and then the pressure corrections. We have designed a test setup for gravity-driven flow (Fig. 8A). The material configuration is similar to that used in Section 5 such that the free surface is curved. All the boundaries are free slip (except

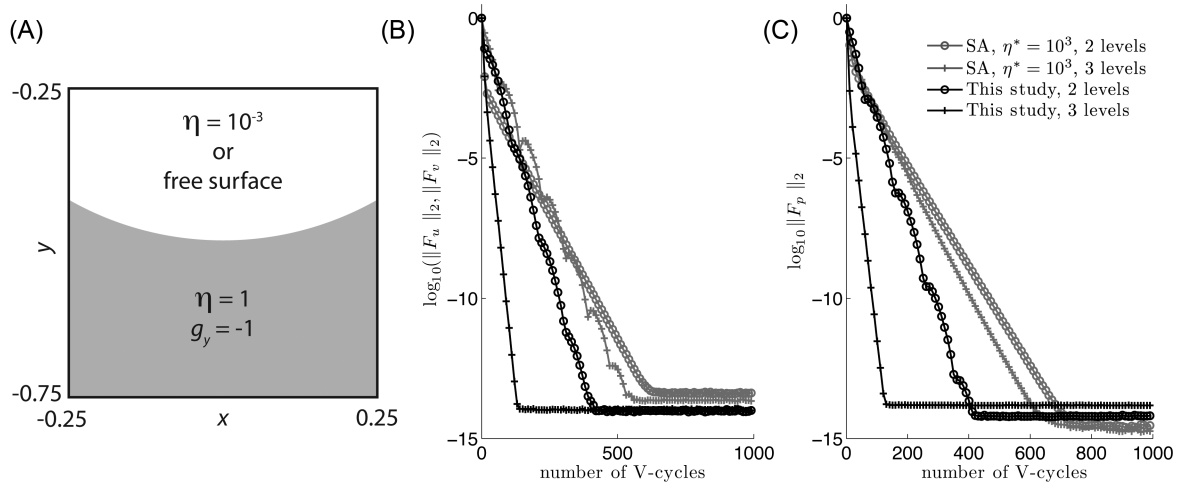

Figure 8. Convergence of an iterative geometric multigrid solver in the presence of a free surface or a sticky air layer (SA models). (A) Model configuration employed for the test. The iterative velocity and pressure residuals are reported in panels (B) and (C), respectively. F_p corresponds to the residual of the continuity equation (divergence). Sticky air and free surface models were run with different smoothing parameters (see Section 8.1.2), which allowed both models to converge at optimal rates.

for the free surface tests) and the models used 50×50 cells (upper cells are deactivated for the free surface cases). The simulations employing sticky air (with $\eta^* = 10^3$) were run with a smoothing relaxation parameter equal to 1.0 and 0.05 for the momentum and continuity equations respectively. However, the free surface simulations, which are iso-viscous, were run with a relaxation parameter equal to 1.0 for both the momentum and continuity equations. Such solver settings allowed both model configurations to converge to machine precision with optimal convergence rates.

We report the results of the convergence of the multigrid solver for both the sticky air and the free surface case in the L_2 norm (Figs 8B and C). In general, models using a free surface boundary condition converge faster that those using a sticky air approximation since they do not require any large viscosity contrast across the free surface. In the experiments performed with a three level multigrid hierarchy, the free surface models converged $\sim$5 times faster than those using sticky air. We hence expect our free surface treatment will be beneficial to 3-D models which employ an iterative flow solver.

8.2 Limitations

The proposed free surface representation suffers from a number of caveats. The discretization of the free surface boundary condition does not conform to the free surface interface, hence the method is limited to being first order accurate in the L_1 norm. In terms of discretization the staircase free surface approach is similar to having a sharp material jump across a control volume, in other words the pressure discretization errors located along the surface will not converge in the L_∞ norm (see Deubelbeiss & Kaus 2008). This is however acceptable for modelling geophysical flows since the absolute value of the dynamic pressures close the Earth's surface are relatively small.

For the time dependent free surface models shown here, our choice of a Lagrangian marker chain to discretize the evolving free surface interface is not ideal as (i) it does not naturally extend to 3-D implementations, (ii) it implicitly assumes that the interface remains a continuous, unbroken line connecting the left and right boundaries. For large deformations of the free surface, maintaining continuity with the marker chain approach may lead to prohibitive computational cost. Using an alternative interface tracking scheme such as level sets would alleviate these two issues. We also note that the discretization of the free surface boundary condition naturally permits multiple closed, unconnected interfaces to exists within a single computational domain, in case several internal free surfaces need to be modelled.

9 CONCLUSIONS

We have developed and tested an alternative free surface boundary condition discretization for geodynamic codes employing a staggered grid finite difference. The method approximates the geometry of free surface on an Eulerian grid via a staircase representation. We have demonstrated that the proposed free surface discretization converges with increasing grid resolution and is first order accurate in space. In order to treat time-dependent flow problems, we proposed an algorithm for tracking the location of the free surface based on a Lagrangian marker chain approach. We have verified our methodology by performing several community benchmarks. Results obtained from our method show good agreement with the community reference models for both the topography evolution and the internal lithosphere/mantle dynamics. Our new methodology represents a promising alternative over the extensively used sticky air approximation since it overcomes several of its major drawbacks, namely (i) the method does not require arbitrary choices to be made for material properties associated with a fictitious fluid, (ii) the proposed free surface discretization converges towards the true free surface boundary condition under mesh refinement and (iii) the method does not deteriorate the convergence of iterative solvers. Our approach hence yields a more accurate representation of free surface boundary condition while simultaneously reducing computational cost (i.e. both in terms of CPU time and memory). Lastly, the stencil modifications required to impose the free surface boundary condition can also be readily extended to 3-D.

ACKNOWLEDGEMENTS

Thanks to Harro Schmeling and Boris Kaus for providing reference data for Figs 6 and 7. The authors acknowledge Taras Gerya and Anton Popov for stimulating discussions. The authors acknowledge Henri Samuel and Harro Schmeling for their detailed and insightful reviews and advices. The authors also thank the editor Stéphane Labrosse for handling the manuscript.

REFERENCES

Braun, J. & Yamato, P., 2010. Structural evolution of a three-dimensional, finite-width crustal wedge, *Tectonophysics,* **484**(1–4), 181–192.

Crameri, F. *et al.*, 2012a. A comparison of numerical surface topography calculations in geodynamic modelling: an evaluation of the 'sticky air' method, *Geophys. J. Int.,* **189**(1), 38–54.

Crameri, F., Tackley, P.J., Meilick, I., Gerya, T.V. & Kaus, B.J.P., 2012b. A free plate surface and weak oceanic crust produce single-sided subduction on earth, *Geophys. Res. Lett.,* **39**(3), L03306, doi:10.1029/2011GL050046.

Deubelbeiss, Y. & Kaus, B., 2008. Comparison of Eulerian and Lagrangian numerical techniques for the Stokes equations in the presence of strongly varying viscosity, *Phys. Earth planet. Inter.,* **171**(1–4), 92–111.

Duretz, T., Gerya, T.V. & May, D.A., 2011a. Numerical modelling of spontaneous slab breakoff and subsequent topographic response, *Tectonophysics,* **502**(1–2), 244–256.

Duretz, T., May, D.A., Gerya, T.V. & Tackley, P.J., 2011b. Discretization errors and free surface stabilization in the finite difference and marker-in-cell method for applied geodynamics: a numerical study, *Geochem. Geophys. Geosyst.,* **12**(7), Q07004, doi:10.1029/2011GC003567.

Fullsack, P., 1995. An arbitrary Lagrangian-Eulerian formulation for creeping flows and its application in tectonic models, *Geophys. J. Int.,* **120**(1), 1–23.

Furuichi, M., May, D.A. & Tackley, P.J., 2011. Development of a Stokes flow solver robust to large viscosity jumps using a Schur complement approach with mixed precision arithmetic, *J. Comput. Phys.,* **230,** 8835–8851.

Gerya, T.V., 2010. *Introduction to Numerical Geodynamic Modelling,* Cambridge Univ. Press.

Gurnis, M., Eloy, C. & Zhong, S., 1996. Free-surface formulation of mantle convection–II. Implication for subduction-zone observables, *Geophys. J. Int.,* **127**(3), 719–727.

Hager, B.H., Clayton, R.W., Richards, M.A., Comer, R.P. & Dziewonski, A.M., 1985. Lower mantle heterogeneity, dynamic topography and the geoid, *Nature,* **313**(6003), 541–545.

Harlow, F.H. & Welch, E., 1965. Numerical calculation of time-dependent viscous incompressible flow of fluid with free surface, *Physics of Fluids,* **8**(12), 2182–2189.

Hillebrand, B., Thieulot, C., Geenen, T., van den Berg, A.P. & Spakman, W., 2014. Using the level set method in geodynamical modeling of multi-material flows and Earth's free surface, *Solid Earth,* **5**(2), 1087–1098.

Kaus, B., 2010. Factors that control the angle of shear bands in geodynamic numerical models of brittle deformation, *Tectonophysics,* **484**(1–4), 36–47.

Kaus, B.J.P., Mühlhaus, H. & May, D.A., 2010. A stabilization algorithm for geodynamic numerical simulations with a free surface, *Phys. Earth planet. Inter.,* **181,** 12–20.

May, D.A. & Moresi, L., 2008. Preconditioned iterative methods for Stokes flow problems arising in computational geodynamics, *Phys. Earth planet. Inter.,* **171**(1–4), 33–47.

McKenzie, D., 1977. Surface deformation, gravity anomalies and convection, *Geophys. J. R. astr. Soc.,* **48**(2), 211–238.

Poliakov, A. & Podladchikov, Y., 1992. Diapirism and topography, *Geophys. J. Int.,* **109**(3), 553–564.

Samuel, H. & Evonuk, M., 2010. Modeling advection in geophysical flows with particle level sets, *Geochem. Geophys. Geosyst.,* **11**(8), Q08020, doi:10.1029/2010GC003081.

Schmalholz, S.M., 2006. Scaled amplification equation: a key to the folding history of buckled viscous single-layers, *Tectonophysics,* **419**(1–4), 41–53.

Schmeling, H. *et al.*, 2008. A benchmark comparison of spontaneous subduction models - towards a free surface, *Phys. Earth planet. Inter.,* **171**(1–4), 198–223.

Schmid, D.W. & Podladchikov, Y.Y., 2003. Analytical solutions for deformable elliptical inclusions in general shear, *Geophys. J. Int.,* **155**(1), 269–288.

Shin, D. & Strikwerda, J.C., 1997. Inf-sup conditions for finite-difference approximations of the Stokes equations, *J. Aust. Math. Soc. B,* **39,** 121–134.

Suckale, J., Nave, J.-C. & Hager, B.H., 2010. It takes three to tango: 1. Simulating buoyancy-driven flow in the presence of large viscosity contrasts, *J. geophys. Res.,* **115**(B7), B07409, doi:10.1029/2009JB006916.

Tackley, P.J., 2008. Modelling compressible mantle convection with large viscosity contrasts in a three-dimensional spherical shell using the yin-yang grid, *Phys. Earth planet. Inter.,* **171**(1–4), 7–18.

van Keken, P.E., King, S.D., Schmeling, H., Christensen, U.R., Neumeister, D. & Doin, M.P., 1997. A comparison of methods for the modeling, *J. geophys. Res.,* **102**(B10), 22 477–22 495.

Weinberg, R.F. & Schmeling, H., 1992. Polydiapirs: multiwavelength gravity structures, *J. Struct. Geol.,* **14**(4), 425–436.

Willett, S.D., 1999. Orogeny and orography: the effects of erosion on the structure of mountain belts, *J. geophys. Res.,* **104**(B12), 28 957–28 981.

Zhong, S., Gurnis, M. & Moresi, L., 1996. Free-surface formulation of mantle convection–I. Basic theory and application to plumes, *Geophys. J. Int.,* **127**(3), 708–718.

SUPPORTING INFORMATION

Additional Supporting Information may be found in the online version of this paper:

FreeSurfaceAccuracyTest.m.
FreeSurfaceInclinedTest.m. (http://gji.oxfordjournals.org/lookup/suppl/doi:10.1093/gji/ggv526/-/DC1).
Please note: Oxford University Press is not responsible for the content or functionality of any supporting materials supplied by the authors. Any queries (other than missing material) should be directed to the corresponding author for the paper.

APPENDIX A: FREE SURFACE TRACKING

In the time-dependent models presented, we have tracked the position of the free surface using a marker chain approach. In the following we describe how we combined the marker chain approach with the Eulerian flow solver.

A1 Surface markers

The free surface interface is represented by a set of Lagrangian marker points (Fig. A1A). The horizontal coordinates x_p of the surface markers is determined by specifying that each control volume containing $\hat{\phi}$ must contain a constant number of surface-markers. The vertical coordinate of each surface marker is defined by evaluating $y_p = \hat{\phi}(x_p)$. The marker chain spacing (proportional to the number of surface markers per cell column) defines the resolution of the marker chain. This marker-based free surface representation will be used to track the position of the free surface through time.

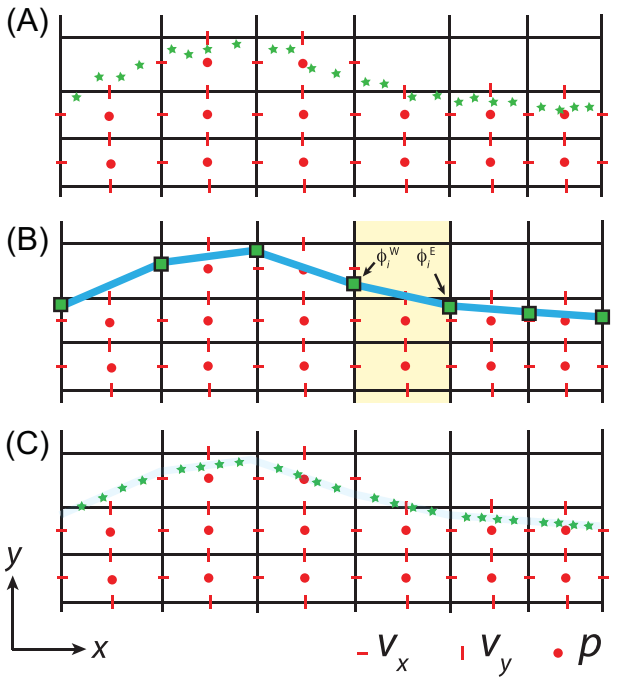

Figure A1. Surface markers and remeshing procedure. (A) Position of the free surface markers (green stars) after an arbitrary number of time steps. (B) Interpolation of the topography from the surface markers to the vertex-based topographic nodes (green squares). The construction of piecewise linear topographic function ($\hat{\phi}$) for each surface cell is denoted by the blue line. (C) Regularly spaced redistribution of surface markers using a new topography value calculated from the piecewise linear function $\hat{\phi}(x)$.

A2 Evaluation of the topographic function

A grid-based representation of the free surface is required in order to discretize the Stokes equations for the current free surface position. For each cell column i, we represent the free surface by a piece-wise linear function. The discrete representation of the approximate the topographic function, $\hat{\phi}(x)$ is thus given by

$$\hat{\phi}(x) = a_i x + b_i, \quad x \in \left[x_i^{\mathrm{W}}, x_i^{\mathrm{E}}\right], \tag{A1}$$

where a_i and b_i are the cell-wise defined coefficients describing the straight line segment and $x_i^{\mathrm{W,E}}$ corresponds to the x-coordinate of the west/east cell edge. The coefficients a_i, b_i are constructed in manner which yields a C_0 continuous approximation to $\phi(x)$. The coefficients are obtained by first projecting the topography from the marker chain onto the location of the vertical grid lines. The procedure is carried out by standard distance-weighted linear interpolation (Gerya 2010). For each cell column we obtain the height of the topography on both the west (ϕ_i^{W}) and east (ϕ^{E}) cell edges. The slope can thus be evaluated as

$$a_i = \frac{\phi_i^{\mathrm{E}} - \phi_i^{\mathrm{W}}}{x_i^{\mathrm{E}} - x_i^{\mathrm{W}}}, \tag{A2}$$

and the intercept is defined as:

$$b_i = \phi_i^{\mathrm{W}} - a_i x_i^{\mathrm{W}}. \tag{A3}$$

An illustration of the continuous nature of $\hat{\phi}(x)$ across cell edges is depicted in Fig. A1(B). Once the topographic function has been evaluated, it is straightforward to proceed to cell flagging (Section 4.1) using the column-wise definition of $\hat{\phi}$ and then subsequently applying the spatial discretization (Section 4.2).

A3 Velocity interpolation and advection

After obtaining the solution of the linear system of equations, the free surface position is evolved using the current flow field. We use an explicit fourth order in space Runge–Kutta solver to advect the Lagrangian surface markers. Each Runge–Kutta step necessitates the projection of the grid-based velocity field onto the location of the markers. For this purpose, we use a standard bilinear node to marker interpolation (Gerya 2010). Similar advection and velocity projection routines are employed to advect the Lagrangian markers corresponding to the material fields, which are located below the surface. One may note that no Lagrangian marker points are needed above the current surface position (defined by $\hat{\phi}(x)$) since this part of the domain is out of the calculation domain.

A4 Remeshing

During the advection step, the surface markers move both vertically and horizontally. As a result, the horizontal marker spacing may become strongly variable and it becomes useful to either remesh the marker chain or add surface markers in regions of strong surface deformation. Here we opted for a two-step marker remeshing procedure. In the first step, we evaluate the topographic function based on the updated surface marker positions. In a second, we reset the horizontal coordinate of the surface markers (e.g. using regular spacing) and we redefine the vertical coordinate of the surface markers based on its horizontal coordinate and the topographic function of the corresponding cell column (Fig. A1C). In the presented application, remeshing was applied at each time step. The remeshing naturally introduces minor numerical diffusion of the topography.

APPENDIX B: AN INCLINED SURFACE

We consider gravity driven flow of a fluid due to a linear inclination of the free surface (i.e. constant slope c). Relationships relating

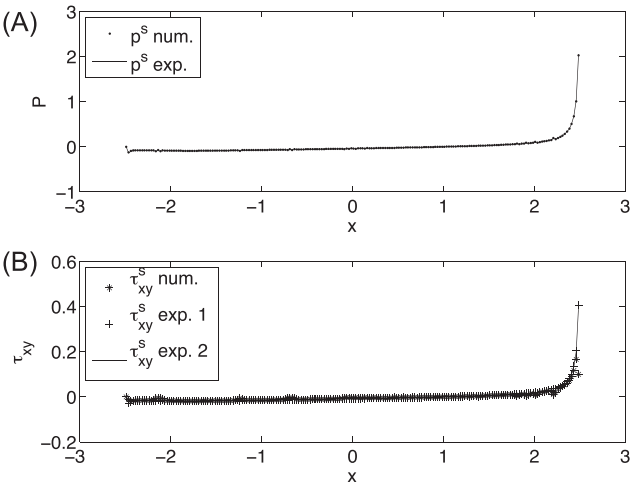

Figure B1. Pressure and shear stress relationships along an inclined plane. The results were obtained using the supplied script (FreeSurfaceInclinedTest.m). Expression for expected pressure (p^s exp.) and shear stress distribution (τ^s_{xy} exp. 1 and 2) are provided in Appendix B.

the pressure, deviatoric normal stress, and shear stress along the inclined free surface can be established using Cauchy's formula. The relation between the pressure and the horizontal deviatoric stress is

$$p^s = \tau^s_{xx} \frac{c^2 + 1}{c^2 - 1}. \tag{B1}$$

The relationship that links shear stress to the deviatoric normal stress is

$$\tau^s_{xy} = \tau^s_{xx} \frac{2c}{1 - c^2}. \tag{B2}$$

This test can reproduced using the supplied script (FreeSurfaceInclinedTest.m). Alternatively the shear stress can expressed as a function of the pressure such that

$$\tau^s_{xy} = -p^s \frac{2c}{c^2 + 1}. \tag{B3}$$

In Fig. B1, we compare numerical pressure and shear stress distributions against semi-analytic predictions. We use numerical values of deviatoric normal stress and pressure (evaluated just below the free surface), to predict the pressure (p^s exp.) and shear stress (τ^s_{xy} exp. 1 and 2) with the above listed relationships. A good qualitative match between expected profiles and numerical solutions is obtained.